A Three-Level Neutral-Point-Clamped Converter Based Standalone Wind Energy Conversion System Controlled with a New Simplified Line-to-Line Space Vector Modulation

Tarak Ghennam, Lakhdar Belhadji, Nassim Rizoug, Bruno Francois, Seddik Bacha

To cite this version:

Tarak Ghennam, Lakhdar Belhadji, Nassim Rizoug, Bruno Francois, Seddik Bacha. A Three-Level Neutral-Point-Clamped Converter Based Standalone Wind Energy Conversion System Controlled with a New Simplified Line-to-Line Space Vector Modulation. Energies, 2024, 17 (9), pp.2214. 10.3390/en17092214 . hal-04639835

HAL Id: hal-04639835
https://hal.science/hal-04639835v1

energies

MDPI

Article

A Three-Level Neutral-Point-Clamped Converter Based Standalone Wind Energy Conversion System Controlled with a New Simplified Line-to-Line Space Vector Modulation [†]

Tarak Ghennam [1], Lakhdar Belhadji [1], Nassim Rizoug [2], Bruno Francois [3] and Seddik Bacha [4,*]

[1] Laboratoire d'Electronique de Puissance, UER-ELT, Ecole Militaire Polytechnique (EMP), BP 17 Bordj-El-Bahri, Alger 16111, Algeria; t_ghennam@yahoo.fr (T.G.); lakhdarbelhadji@gmail.com (L.B.)
[2] Ecole Supérieure des Techniques Aéronautiques et de Construction Automobile (ESTACA), BP 76121, 53061 Laval, France; nassim.rizoug@estaca.fr
[3] Laboratoire d'Electrotechnique et d'Electronique de Puissance de Lille (L2EP), Centrale Lille, Cité Scientifique, BP 48, 59651 Villeneuve d'Ascq, France; bruno.francois@centralelille.fr
[4] Grenoble INP, Université de Grenoble Alpes, CNRS, G2Elab, 38000 Grenoble, France
* Correspondence: seddik.bacha@g2elab.grenoble-inp.fr

[†] This paper is an extended version of our paper published in the 21st European Conference on Power Electronics and Applications (EPE'19 Europe), Genova, Italy, 3–5 March 2019.

Abstract: Wind power systems, which are currently being constructed for the electricity worldwide market, are mostly based on Doubly Fed Induction Generators (DFIGs). To control such systems, multilevel converters are increasingly preferred due to the well-known benefits they provide. This paper deals with the control of a standalone DFIG-based Wind Energy Conversion System (WECS) by using a three-level Neutral-Point-Clamped (NPC) converter. The frequency and magnitude of the stator output voltage of the DFIG are controlled and fixed at nominal values despite the variable rotor speed, ensuring a continuous AC supply for three-phase loads. This task is achieved by controlling the DFIG rotor currents via a PI controller combined with a new Simplified Direct Space Vector Modulation strategy (SDSVM), which is applied to the three-level NPC converter. This strategy is based on the use of a line-to-line three-level converter space vector diagram without using Park transformation and then simplifying it to that of a two-level converter. The performance of the proposed SDSVM technique in terms of controlling the three-level NPC-converter-based standalone WECS is demonstrated through simulation results. The whole WECS control and the SDSVM strategy are implemented on a dSPACE DS 1104 board that drives a DFIG-based wind system test bench. The obtained experimental results confirm the validity and performance in terms of control.

Keywords: standalone wind energy conversion system; doubly fed induction generator; three-level neutral-point-clamped converter; AC supply control; simplified direct space vector modulation strategy

check for updates

Citation: Ghennam, T.; Belhadji, L.; Rizoug, N.; Francois, B.; Bacha, S. A Three-Level Neutral-Point-Clamped Converter Based Standalone Wind Energy Conversion System Controlled with a New Simplified Line-to-Line Space Vector Modulation. *Energies* **2024**, *17*, 2214. https://doi.org/10.3390/en17092214

Academic Editor: Alon Kuperman

Received: 16 December 2023
Revised: 12 April 2024
Accepted: 16 April 2024
Published: 4 May 2024

1. Introduction

Recently, there has been a strong trend toward wind energy utilization either for grid connection or for household supply [1–3]. Hence, new wind generators of several MW have been developed and are currently being installed worldwide for use in high-power wind generation systems [4–6]. In these power systems, DFIGs are more commonly used due to their variable speed operating abilities, with four-quadrant active and reactive power capabilities [2,7]. Furthermore, the PWM converters that are in use are designed to flow only the slip power, which is roughly 30% of the nominal generated electricity, thanks to the reduced power flowed by the rotor windings of a DFIG [7,8].

Despite the advantages in terms of reducing the PWM converter rating, the increased power of recent wind turbines requires the use of parallel connections of several back-to-back two-level converter modules to increase the transferred total power [7,9]. Hence, high power is transferred by the current rather than the voltage and, as a result, the high current can be handled and greater power losses in the conversion systems are achieved.

In order to enhance system yield and reduce the power loss in these conversion systems, multilevel PWM converters are increasingly preferred due to the advantages that they provide [10,11]. In fact, they increase the power rating thanks to their increased output-modulated voltages since the blocking voltage of each switch is one-half that of the DC link voltage [9–12]. Furthermore, their output voltage waveform is improved and, consequently, the voltage harmonic content is reduced compared to that of two-level converters with the same switching frequency [13,14].

To control these converters, many control strategies have been proposed and developed [12,15–18]. Three-hysteresis comparator control has been considered the simplest control strategy, but it suffers from high-frequency operation and phase current interactions [12]. The Carrier-Based Modulation (CBM) method uses a combination of a triangular carrier and a phase reference signal. Hence, a complex analog circuit is required. Nevertheless, devices have to be added to the CBM to balance the DC link voltage. In addition to this, interference between the three phases can be created since each phase is controlled separately. Contrary to this, Space Vector Modulation (SVM) strategies gather the three phase references in one entity to avoid phase interference, but most of them employ complex dwelling time computation due to the use of complicated transformations, especially for multilevel inverters.

This paper presents a new SDSVM for a three-level NPC-converter-based standalone WECS (Figure 1) to control the frequency and magnitude of DFIG stator output voltages supplying an isolated load. The advantage of this proposed SDSVM compared to the CBM is the fact that it can gather the three phase reference signals into one entity vector without any complex analog circuitry, avoiding interference between the three phases. Similarly, its advantage compared to other conventional SVM strategies is the fact that it enables, on the one hand, the copying of directly modulated waveforms onto output voltages of a three-phase, three-level converter without using a Park transformation. On the other hand, it allows for the simplification of the line-to-line space vector diagram of a three-level converter into that of a two-level one. Therefore, the SDSVM algorithm is implemented more easily and, hence, the execution time is greatly reduced since it uses an easy time calculation based on a simple subtraction rather than a complicated matrix transformation. In addition to this, the feasibility of the SDSVM strategy for the control of the three-level-based standalone WECS is studied and analyzed for a continuous AC supplying a three-phase load.

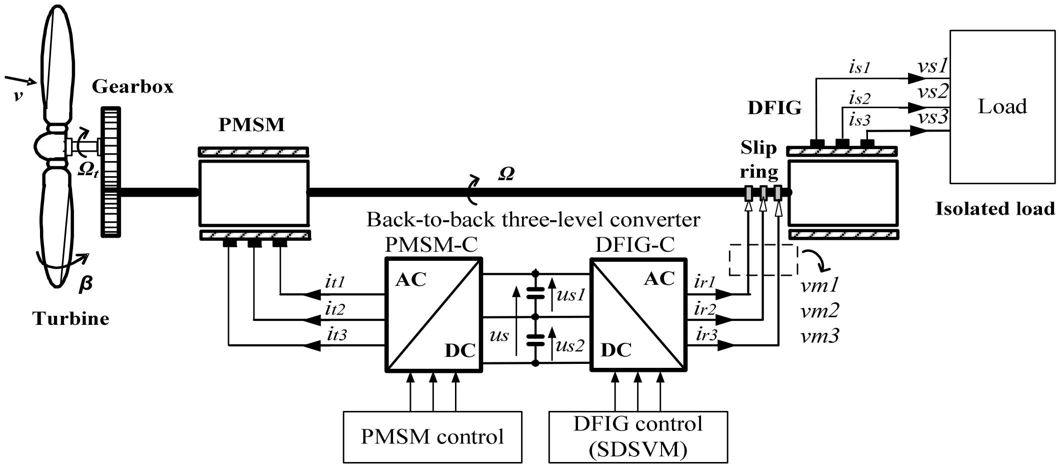

Figure 1. The figure shows the wind conversion system.

This paper is organized as follows: in the Section 2, we briefly present the constitution and operation of the WECS. The Section 3 is devoted to the line-to-line modeling of the three-level NPC converter as well as the modeling of the DFIG. The Section 4 presents the macroscopic control of the standalone WECS with a focus on the proposed SDSVM algorithm. Finally, the Sections 5 and 6 are dedicated, respectively, to proving the validity and efficiency of the proposed scheme through simulations and experimental results.

2. Standalone WECS Presentation

A representation of the standalone WECS when feeding an isolated load is given in Figure 1. It is composed of a small-scale wind turbine coupled to a Permanent Magnet Synchronous Machine (PMSM) and DFIG through a gearbox. The back-to-back three-level NPC converter is connected to the PMSM to provide the appropriate DC link voltage, and it is also linked to an isolated load that provides the required supply of electricity. Thus, the DFIG-side converter controls the frequency and magnitude of the stator output voltage of the DFIG in order to ensure a continuous AC supply for the three-phase load, whereas the PMSM-side converter controls the DC link voltage. This paper deals mainly with DFIG control via a three-level NPC converter, focusing on the application of the proposed SDSVM technique. Thus, the next section concerns the modeling of both the three-level NPC converter and the DFIG.

3. Standalone WECS Modeling

3.1. Line-to-Line Conversion Modeling of the Three-Level NPC Converter

Figure 2 demonstrates the structure of the DFIG-side three-level NPC converter, which consists of three commutation circuits fed by a capacitive voltage divider. The voltage across the two capacitors, u_{s1} and u_{s2}, must be controlled to be equal to half the value of the full DC voltage u_s to ensure the good operation of the NPC converter.

$$u_{s1} = u_{s2} = \frac{u_s}{2} \tag{1}$$

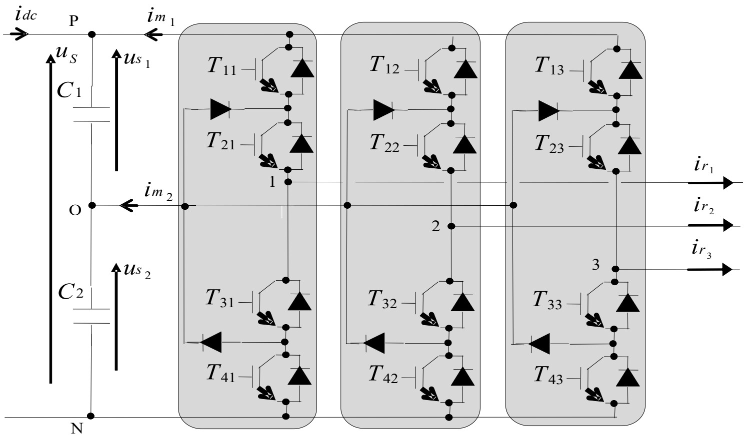

Figure 2. The figure shows the structure of the used three-level NPC converter.

Line-to-line voltage (u_{m1}, u_{m2}) modeling of the DFIG-side three-level NPC converter is now detailed and will be used by the proposed SDSVM rather than voltage coordinates in the αβ reference frame.

The first clamped commutation circuit (Figure 3a) is considered in order to present the operating of the NPC converter.

- In the case where the switches T_{1c} and T_{2c} are on, the output voltage v_{m1} is equal to u_s.
- In the case where the switches T_{2c} and T_{3c} are on, the output voltage v_{m1} is equal to $u_{s1} = u_s/2$.
- In the case where the switches T_{3c} and T_{4c} are on, the output voltage v_{m1} is equal to 0.

Therefore, this clamped commutation circuit is equivalent to a commutation circuit whose one ideal switch among the three is at any time switched on (Figure 3b).

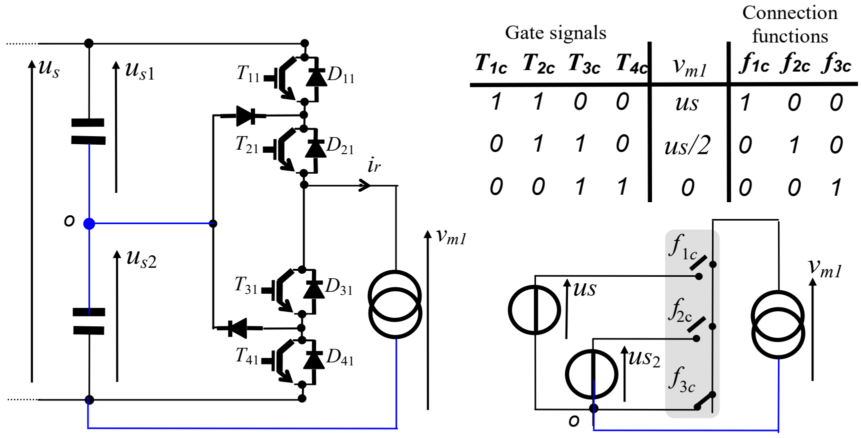

Gate signals T_{1c}	T_{2c}	T_{3c}	T_{4c}	v_{m1}	Connection functions f_{1c}	f_{2c}	f_{3c}
1	1	0	0	us	1	0	0
0	1	1	0	us/2	0	1	0
0	0	1	1	0	0	0	1

(a) (b)

Figure 3. The figure shows an equivalent commutation circuit: (**a**) first clamped commutation circuit; (**b**) first equivalent commutation circuit.

The switch states are modeled using switching functions (f_{rc}). The index r corresponds to a row, and c corresponds to a commutation circuit. If f_{rc} = 1, the corresponding ideal switch (and so a corresponding transistor) is closed. Otherwise, if f_{rc} = 0, it is open. Thus, switching functions in the equivalent commutation circuit depend on transistor gate signals, as follows:

$$f_{1c} = T_{1c}, f_{3c} = T_{4c}, f_{2c} = T_{2c}.T_{3c} \tag{2}$$

All of the ideal switches are represented in a matrix containing vertical equivalent commutation circuits (Figure 4).

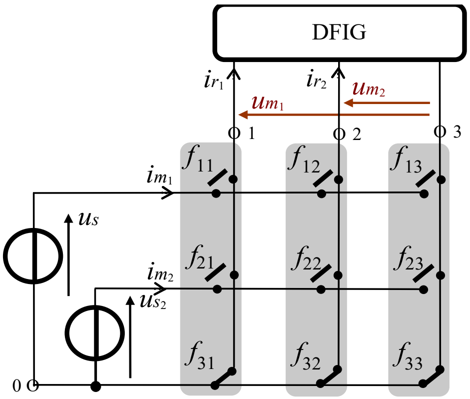

Figure 4. The figure shows a diagram of a matrix converter structure with three commutation cells of three switches.

Only two line-to-line modulated voltages u_{m1} and u_{m2} are considered:

$$\begin{cases} u_{m1} = v_{m1} - v_{m3} = (f_{11} - f_{13})u_s + (f_{21} - f_{23})u_{s2} \\ u_{m2} = v_{m2} - v_{m3} = (f_{12} - f_{13})u_s + (f_{22} - f_{23})u_{s2} \end{cases} \tag{3}$$

The modulated currents i_{m1} and i_{m2} are expressed as follows:

$$\begin{cases} i_{m1} = (f_{11} - f_{13})i_{r1} + (f_{21} - f_{23})i_{r2} \\ i_{m2} = (f_{12} - f_{13})i_{r1} + (f_{22} - f_{23})i_{r2} \end{cases} \tag{4}$$

We define conversion functions (m_{rc}) as follows [19]:

$$\begin{cases} m_{11} = f_{11} - f_{13} \\ m_{12} = f_{12} - f_{13} \\ m_{21} = f_{21} - f_{23} \\ m_{22} = f_{22} - f_{23} \end{cases} \tag{5}$$

$$m_{rc} = f_{rc} - f_{r3} \tag{6}$$

By replacing (5) in Equations (3) and (4) we find the following:

$$\begin{cases} u_{m1} = m_{11}u_s + m_{21}u_{s2} \\ u_{m2} = m_{12}u_s + m_{22}u_{s2} \end{cases} \tag{7}$$

$$\begin{cases} i_{m1} = m_{11}i_{r1} + m_{21}i_{r2} \\ i_{m2} = m_{12}i_{r1} + m_{22}i_{r2} \end{cases} \tag{8}$$

3.2. DFIG Based WECS Modeling

To establish the DFIG model, it is convenient to refer to the electric equations of the rotating Park reference frame that is synchronized with the stator flux (Figure 5) since the DFIG-based WECS presented in this study supplies an isolated load via its stator voltages.

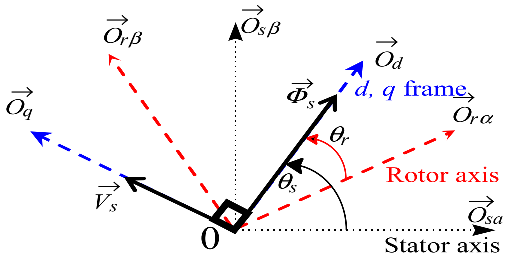

Figure 5. The figure shows the orientation of the d, q frame.

In the Park reference frame, the DFIG stator electric equations are given as follows [8,20–23]:

$$\begin{cases} v_{sd} = R_s i_{sd} + \frac{d\phi_{sd}}{dt} - \omega_s \phi_{sq} \\ v_{sq} = R_s i_{sq} + \frac{d\phi_{sq}}{dt} + \omega_s \phi_{sd} \\ v_{rd} = R_r i_{rd} + \frac{d\phi_{rd}}{dt} - \omega_r \phi_{rq} \\ v_{rq} = R_r i_{rq} + \frac{d\phi_{rq}}{dt} + \omega_r \phi_{rd} \end{cases} \tag{9}$$

The stator and rotor flux are given as follows:

$$\begin{cases} \phi_{sd} = L_s i_{sd} + L_m i_{rd} \\ \phi_{sq} = L_s i_{sq} + L_m i_{rq} \\ \phi_{rd} = L_r i_{rd} + L_m i_{sd} \\ \phi_{rq} = L_r i_{rq} + L_m i_{sq} \end{cases} \tag{10}$$

R_s and L_s are, respectively, the resistances and inductances of the stator windings, and L_m is the mutual inductance.

V_{sd}, v_{sq}, v_{rd}, v_{rq}, i_{sd}, i_{sq}, i_{rd}, i_{rq}, ϕ_{sd}, ϕ_{sq}, ϕ_{rd}, and ϕ_{rq} are the d and q components of the stator and rotor voltages, currents, and flux. ω_r and ω_s are, respectively, the electric rotor and stator pulsations in rad/s.

Rotor speed ω_r is deduced from stator speed ω_s and mechanical speed Ω as follows:

$$\omega_r = \omega_s - p\Omega \tag{11}$$

where Ω is the mechanical speed in rad/s, and p is the pole pair number.

The angle θ_r is obtained by integrating the previous equation

$$\theta_r = \int_{t_0}^{t_0+\Delta t} \omega_r dt + \theta_{r_0} \tag{12}$$

Since the stator flux is oriented with d axis, the following conditions can be set:

$$\begin{cases} \phi_{sq} = \frac{d\phi_{sq}}{dt} = 0 \\ \phi_{sd} = \phi_s \end{cases} \tag{13}$$

Voltage and flux equations of the stator windings can be simplified in a steady state by assuming that the resistance of the stator winding R_s is neglected:

$$\begin{cases} v_{sd} = 0 \\ v_{sq} = v_s = \omega_s \phi_s \end{cases} \tag{14}$$

$$\begin{cases} \phi_{sd} = \phi_s = L_s i_{sd} + L_m i_{rd} \\ \phi_{sq} = 0 = L_s i_{sq} + L_m i_{rq} \end{cases} \tag{15}$$

From Equation (15), the equations relating the stator currents to the rotor currents are given as follows:

$$\begin{cases} i_{sd} = \frac{\phi_s}{L_s} - \frac{L_m}{L_s} i_{rd} \\ i_{sq} = -\frac{L_m}{L_s} i_{rq} \end{cases} \tag{16}$$

From Equations (10) and (16), the following expressions can be deduced:

$$\begin{cases} i_{rq} = -\frac{L_s}{L_m} i_{sq} \\ \phi_{rq} = -\frac{\sigma L_s L_r}{L_m} i_{sq} \end{cases} \tag{17}$$

where $\sigma = 1 - \frac{L_m^2}{L_s L_r}$

$$\begin{cases} v_{rd} = R_r i_{rd} + \sigma L_r \frac{di_{rd}}{dt} - e_q \\ v_{rq} = R_r i_{rq} + \sigma L_r \frac{di_{rq}}{dt} + e_d + e_\phi \end{cases} \tag{18}$$

where

$$\begin{cases} e_q = -\omega_r \sigma L_r i_{rq} \\ e_d = \omega_r \sigma L_r i_{rd} \\ e_\phi = \omega_r \frac{L_m}{L_s} \phi_s \end{cases} \tag{19}$$

4. Standalone WECS Control

4.1. Overall WECS Control

Several recent pieces of research on DFIG-based WECS control techniques can be distinguished [24–27]. In a standalone WECS mode, the frequency and magnitude of the DFIG stator output voltage have to be controlled and should be fixed at nominal values, regardless of the variable rotor speed [28]. Three control stages can be distinguished in the control method (Figure 6): the first control stage is dedicated to regulating the stator voltage magnitude to the desired value V_{s_ref}, while the second control stage is devoted to rotor current control. The third control stage deals with three-level NPC converter control by using the proposed SDSVM technique.

The measured d and q components of the stator voltage (v_{sd}, v_{sq}) are used to calculate the magnitude of the output voltage vector:

$$\|v_s\| = \sqrt{\hat{v}_{sd}^2 + \hat{v}_{sq}^2} \tag{20}$$

The rotor frequency f_r is adjusted somehow to regulate the stator frequency to its nominal value simply by verifying the following equation:

$$f_r = \left| f_s - \frac{p\Omega}{2\pi} \right| \tag{21}$$

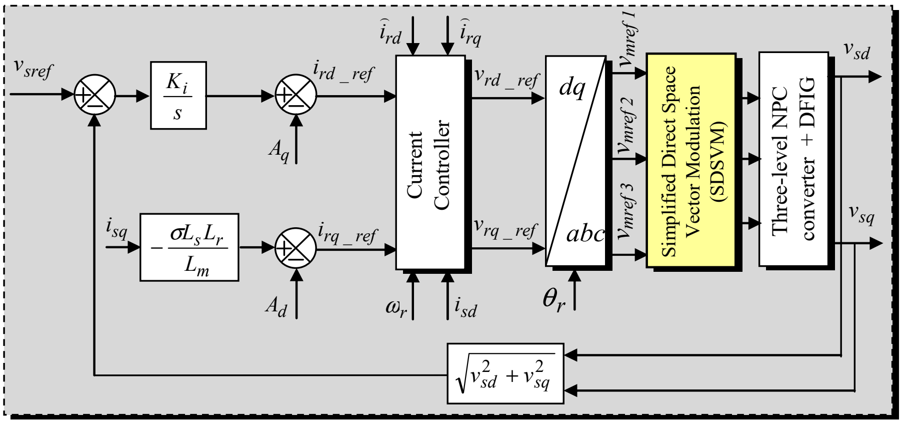

Figure 6. The figure shows a block diagram of standalone DFIG-based WECS control.

Since the control inputs of the DFIG are the rotor currents, it is convenient to express the stator voltage versus the rotor currents, and this is achieved by substituting the stator flux components given in Equation (10) in Equation (9). Thus, the DFIG stator voltages can be rewritten as follows:

$$\begin{cases} v_{sd} = R_s i_{sd} + L_s \frac{di_{sd}}{dt} + L_m \frac{di_{rd}}{dt} - \omega_s \phi_{sq} \\ v_{sq} = R_s i_{sq} + L_s \frac{di_{sq}}{dt} + L_m \frac{di_{rq}}{dt} + \omega_s \phi_{sd} \end{cases} \tag{22}$$

In a steady state, the DFIG stator voltages can be expressed as follows:

$$\begin{cases} v_{sd} = R_s i_{sd} - \omega_s \phi_{sq} \\ v_{sq} = R_s i_{sq} + \omega_s \phi_{sd} \end{cases} \tag{23}$$

The stator resistance is neglected (R_s = 0), and by replacing the stator flux components with the expressions given in Equation (10) in Equation (23), it yields:

$$\begin{cases} v_{sd} = -\omega_s L_m (i_{rq} + A_d) \\ v_{sq} = +\omega_s L_m (i_{rd} + A_q) \end{cases} \tag{24}$$

where

$$\begin{cases} A_d = \frac{R_s}{\omega_s L_m} i_{sd} - \frac{L_s}{L_m} i_{sq} \\ A_q = \frac{R_s}{\omega_s L_m} i_{sq} - \frac{L_s}{L_m} i_{sd} \end{cases} \tag{25}$$

4.2. DFIG Rotor Current Control

The second stage is devoted to the rotor current controller. The rotor currents of the DFIG are sensed and transformed to the *dq* reference frame by using a Park transformation. Then, their control is ensured using two PI controllers (Figure 7) after they are compared to their references. The *d* and *q* components of the DFIG rotor voltage reference v_{rd_ref} and v_{rq_ref} are thus evaluated (Figure 7). Thanks to the modeling provided by Equation (19), the *emf* coupling of $\tilde{e}_{d\_ref}$, $\tilde{e}_{q\_ref}$, and $\tilde{e}_{\Phi\_ref}$ are estimated from the measured rotor and stator currents of the DFIG, rotor current pulsation ω_r and estimated *d* component of the stator flux $\widetilde{\phi}_{sd}$, as follows:

$$\begin{cases} \tilde{e}_{q\_ref} = -L_r\omega_r\sigma\widehat{\mathrm{i}}_{rq} \\ \tilde{e}_{d\_ref} = L_r\omega_r\sigma\widehat{\mathrm{i}}_{rd} \\ \tilde{e}_{\phi\_ref} = \omega_r\frac{L_m}{L_s}\tilde{\phi}_{sd} \end{cases} \tag{26}$$

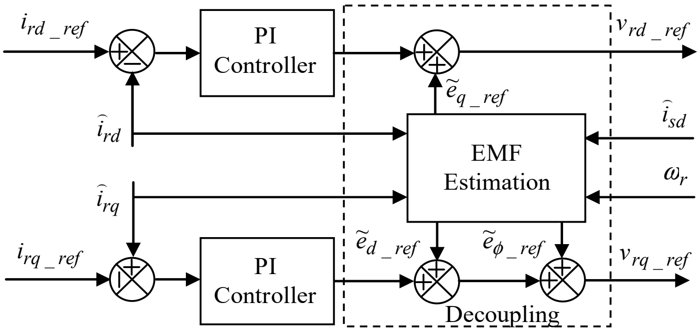

Figure 7. The figure shows the DFIG current controller.

4.3. Simplified Direct Space Vector Modulation (SDSVM)

After controlling the rotor currents, the voltage references v_{rd_ref} and v_{rq_ref} issued from the DFIG rotor current controller (Figure 7) have to be transformed to v_{mref1}, v_{mref2} and v_{mref3} by using Park^{-1} transformation in equilibrium with the three-phase system.

$$\left\{ \begin{bmatrix} v_{mref1} \\ v_{mref2} \\ v_{mref3} \end{bmatrix} = \begin{bmatrix} \cos\theta_r & -\sin\theta_r \\ \cos(\theta_r - 2\pi/3) & -\sin(\theta_r - 2\pi/3) \\ \cos(\theta_r + 2\pi/3) & -\sin(\theta_r + 2\pi/3) \end{bmatrix} \begin{bmatrix} v_{rd\_ref} \\ v_{rq\_ref} \end{bmatrix} \right. \tag{27}$$

The proposed SDSVM strategy has to control the three-level NPC converter in the line-to-line (u_{m1}, u_{m2}) reference frame. The global schematic of the SDSVM (Figure 8) consists of three blocks: hexagon detection, sector detection, and voltage vector selection and duration calculation.

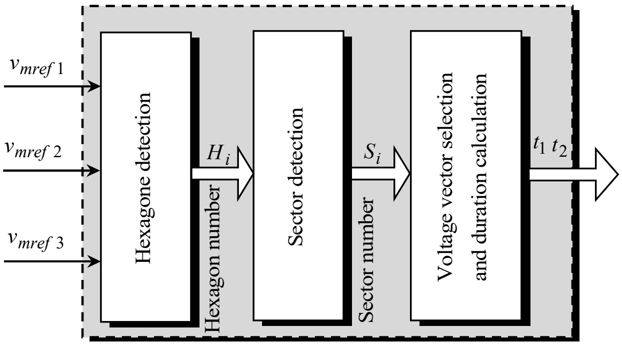

Figure 8. The figure shows a global schematic of the SDSVM.

The main principle of this modulation strategy is to divide the line-to-line space vector diagram of the three-level converter into six small hexagons that are the space vector diagram in the line-to-line reference frame of a conventional two-level inverter (Figure 9). As illustrated, the hexagons (H_1, H_3, H_4, and H_6) shift from the center by $u_s/2$, whereas the hexagons (H_2 and H_5) shift by $\sqrt{2}u_s/2$ [29]. Two procedures must be completed to transform the three-level space vector frame to the two-level space vector frame:

1. Only one hexagon must be selected among the six, and this is performed according to the location of a given reference voltage.
2. The original reference voltage vector must be subtracted from the amount of the center voltage vector of the selected hexagon (Figure 9).

Hence, the determination of the switching sequence and the calculation of the voltage vector duration are carried out for a two-level direct SVM [30].

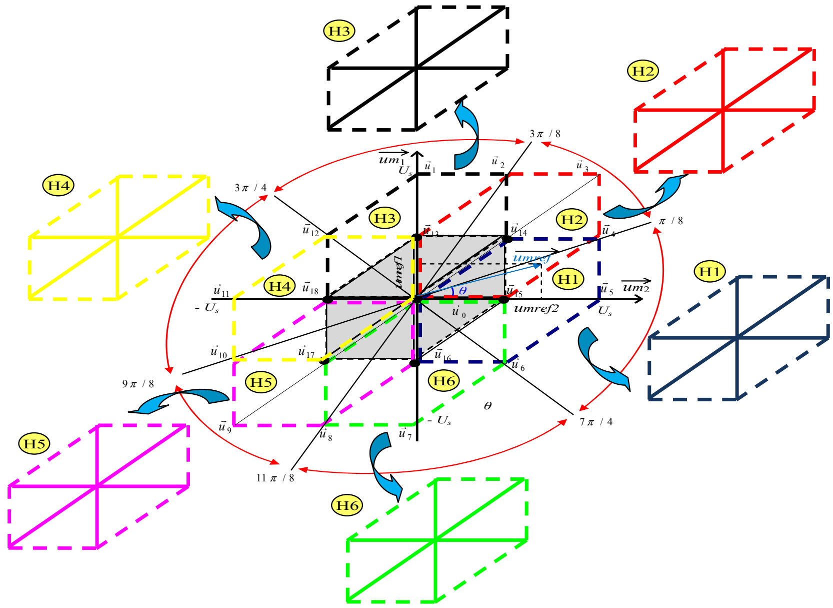

Figure 9. The figure shows a line-to-line space vector diagram of a three-level converter.

4.3.1. Hexagon Detection and Reference Vector Correction

At first, the modulated voltage references v_{mref1}, v_{mref2} and v_{mref3}, issued from Equation (27) have to be transformed into line-to-line voltages.

$$\begin{cases} u_{mref1} = v_{mref1} - v_{mref3} \\ u_{mref2} = v_{mref2} - v_{mref3} \end{cases} \tag{28}$$

Then, the space vector diagram in the frame (u_{m1}, u_{m2}) is divided into six hexagons (H_1–H_6) (Figure 9).

Each hexagon is defined according to the angle θ between the u_{m2}-axis and the reference voltage vector $\vec{u}_{mref}$.

$$\theta = arctg\frac{u_{mref1}}{u_{mref2}} \tag{29}$$

Table 1 gives the conditions that must be satisfied for the reference voltage vector $\vec{u}_{mref}$ to belong to each particular hexagon. Once the small hexagon is detected, the correction of the voltage vector should be performed by considering the hexagon number H_i.

1. In the case where the reference voltage vector $\vec{u}_{mref}$ belongs to one of the following hexagons (H_1 or H_3 or H_4 or H_6), then the new corrected reference voltage vector $\vec{u}_{mref\_c}$ is given as follows:

$$\vec{u}_{mref\_c} = \vec{u}_{mref} + \vec{u}_s/2 \tag{30}$$

2. In the case where the reference voltage vector $\vec{u}_{mref}$ belongs to one of the following hexagons (H_2 or H_5), then the new corrected reference voltage vector $\vec{u}_{mref\_c}$ is given as follows:

$$\vec{u}_{mref\_c} = \vec{u}_{mref} + \sqrt{2}\vec{u}_s/2 \tag{31}$$

Table 1. The table shows hexagon detection.

Angle θ	**Hexagon (H)**
$7\pi/4 < \theta < \pi/8$	H_1
$\pi/8 < \theta < 3\pi/8$	H_2
$3\pi/8 < \theta < 3\pi/4$	H_3
$3\pi/4 < \theta < 9\pi/8$	H_4
$9\pi/8 < \theta < 11\pi/8$	H_5
$11\pi/8 < \theta < 7\pi/4$	H_6

4.3.2. Sector Detection

Once the hexagon is identified and the voltage vector corrected, the sector should be identified in the same way, according to the angle θ_c between the u_{m2}-axis and the new reference voltage vector $\vec{u}_{mref\_c}$ (Figure 10). Thus, six triangular sectors ($S_1 - S_6$) can be distinguished.

$$\theta_c = arctg\frac{u_{mref1\_c}}{u_{mref2\_c}} \tag{32}$$

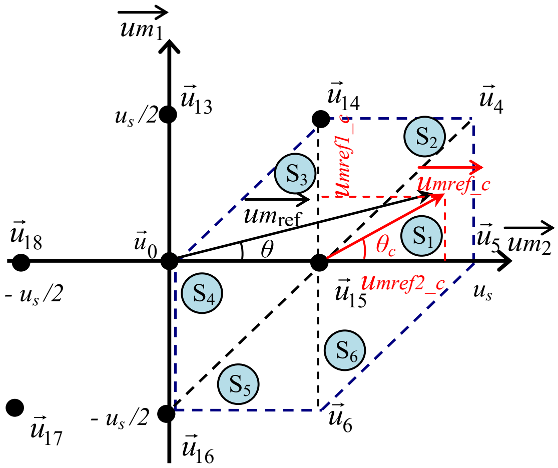

Figure 10. The figure shows the corrected reference voltage vector in hexagon H_1.

Table 2 gives the conditions that must be satisfied for the reference voltage vector $\vec{u}_{mref\_c}$ to belong to each particular sector S_i.

Table 2. The table shows sector detection.

Angle θ_c	**Sector (S)**
$0 < \theta_c < \pi/4$	S_1
$\pi/4 < \theta_c < \pi/2$	S_2
$\pi/2 < \theta_c < \pi$	S_3
$\pi < \theta_c < 3\pi/4$	S_4
$5\pi/4 < \theta_c < 3\pi/2$	S_5
$3\pi/2 < \theta_c < 2\pi$	S_6

4.3.3. Voltage Vector Selection and Duration Calculation

In this stage, the proposed SDSVM strategy uses the nearest two voltage vectors. Therefore, the choice of the two selected voltage vectors has to be modified according to hexagon H_i first and then sector S_i, where the reference voltage vector is located.

The duration of each vector is determined by the obtained projections onto the frame vectors (u_{m1}, u_{m2}). For example, for a desired modulation vector located in sector S_1 (Figure 11), the three selected vectors are $\vec{u}_5$, $\vec{u}_4$, and $\vec{u}_0$ *or* $\vec{u}_7$. Their respective durations (t_1, t_2, and t_0) and the modulation time T_m are expressed according to the following:

$$\overrightarrow{u}_{mref\_c} = \frac{t_1}{T_m}\overrightarrow{u}_5 + \frac{t_2}{T_m}\overrightarrow{u}_4 + \frac{t_0}{T_m}\overrightarrow{u}_0 \tag{33}$$

In fact, only two durations must be determined because all durations must be equal to the modulation period:

$$T_m = t_1 + t_2 + t_0 \tag{34}$$

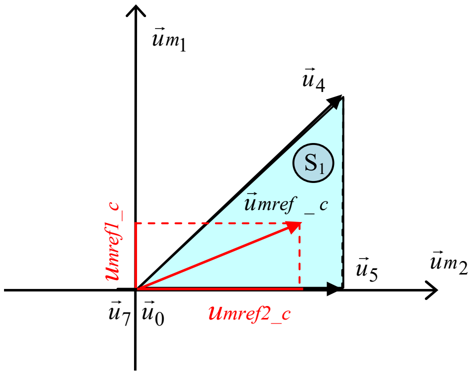

Figure 11. The figure shows an expanded view of the studied sector S_1.

In order to obtain parallel projections with vectors $\overrightarrow{u}_{m1}$ and $\overrightarrow{u}_{m2}$, the duration of the zero vector will always be determined according to the others. For our example, we achieved the following:

$$\overrightarrow{u}_{mref\_c} = \frac{t_1}{T_m}\overrightarrow{u}_5 + \frac{t_2}{T_m}\overrightarrow{u}_4 + \frac{(T_m - t_1 - t_2)}{T_m}\overrightarrow{u}_0 \tag{35}$$

The above equation can be rewritten as follows:

$$\overrightarrow{u}_{mref\_c} = \frac{t_1}{T_m}(\overrightarrow{u}_5 - \overrightarrow{u}_0) + \frac{t_2}{T_m}(\overrightarrow{u}_4 - \overrightarrow{u}_0) + \overrightarrow{u}_0 \tag{36}$$

Using the projection already mentioned on the u_{m1}-axis and u_{m2}-axis, we obtain the following:

On the u_{m1}-axis:

$$\begin{cases} u_5 - u_0 = 0 \\ u_4 - u_0 = \sqrt{2}u_s \end{cases} \tag{37}$$

On the u_{m2}-axis:

$$\begin{cases} u_5 - u_0 = u_s \\ u_4 - u_0 = \sqrt{2}u_s \end{cases} \tag{38}$$

Hence, the durations t_1 and t_2 are obtained using (36)–(38), as follows:

$$\begin{cases} t_1 = \frac{u_{mref2\_c} - u_{mref1\_c}}{u_s}T_m \\ t_2 = \frac{\sqrt{2}u_{mref1\_c}}{u_s}T_m \end{cases} \tag{39}$$

We assume that

$$\begin{cases} X = \frac{u_{mref2\_c}}{u_s}T_m \\ Y = \frac{u_{mref1\_c}}{u_s}T_m \end{cases} \tag{40}$$

Therefore, the durations of t_1, t_2, and t_0 are given as follows:

$$\begin{cases} t_1 = X - Y \\ t_2 = \sqrt{2}Y \\ t_0 = T_m - t_1 - t_2 \end{cases} \quad (41)$$

The calculation of the durations t_1 and t_2 in the six sectors are summarized in Table 3 [29].

Table 3. The table shows the duration calculation for hexagon H_1.

t/S	S_1	S_2	S_3	S_4	S_5	S_6
t_1	X-Y	$\sqrt{2}X$	Y	Y-X	$-\sqrt{2}X$	$-Y$
t_2	$\sqrt{2}Y$	Y-X	$-X$	$-\sqrt{2}Y$	X-Y	X

For the five remaining hexagons (H_2–H_6), the duration calculation can be established in the same way. The use of redundant voltage vectors allows for DC link voltage balancing [12,14,19] according to the sign of Δu_s ($u_{s1} - u_{s2}$) and the sign of the three rotor currents of the DFIG.

5. Simulation Results

In order to verify the theoretical study of the three-level NPC-converter-based standalone WECS controlled with the proposed SDSVM strategy, the numerical simulation of the complete standalone DFIG-based WECS and its control has been performed by using MATLAB/Simulink software 2013b. The simulation results were obtained using the following elements: a DFIG with a 6 kVA three-level converter; f = 5 kHz; capacitors C_1 = C_2 = 750 µF; a three-phase load of R_l = 30 Ω; L_l = 5 mH; and DC link voltage of u_s = 600 V.

Figure 12a shows that the overall WECS system is well controlled since the measured output voltage is well regulated to its reference despite variations in the rotating speed of the wind turbine, which varies from 1000 rpm to 2000 rpm (Figure 12b). The good regulation is confirmed by the small value of the mean square error of the observed variable V_s with respect to the reference V_{s_ref}, which is equal to 0.25. The voltages u_{s1} and u_{s2} across the capacitors C_1 and C_2 are equal (Figure 12c); hence, the DC link voltage is balanced. This result confirms that the proposed SDSVM scheme adheres to the redundant converter switching states. Figure 12d displays the reference-modulated voltages and the voltage vectors used for the three-level NPC converter that are drawn in the plan (u_{m1}, u_{m2}). Figure 12e,f illustrates the modulated line-to-line output voltage of the three-level NPC converter and its respective single-sided amplitude spectrum. The calculated THD of the modulated line-to-line output voltage is −30.034.

In order to test the robustness of the overall control system, Figure 13 demonstrates the simulation results of standalone WECS control with load variation. In fact, a scenario that simulates the connection and disconnection of a second load at times t = 0.5 s and t = 1.5 s, respectively, is considered. Figure 13a shows that the DFIG stator output voltage is well regulated even during the connection or disconnection of other loads. Figure 13b illustrates the active and reactive powers produced by the DFIG and consumed by the three-phase load during this transient time. The three-phase load currents and also their zoom are displayed in Figure 13c,d. The results presented in this figure prove the robustness of the overall control system, even with load variation.

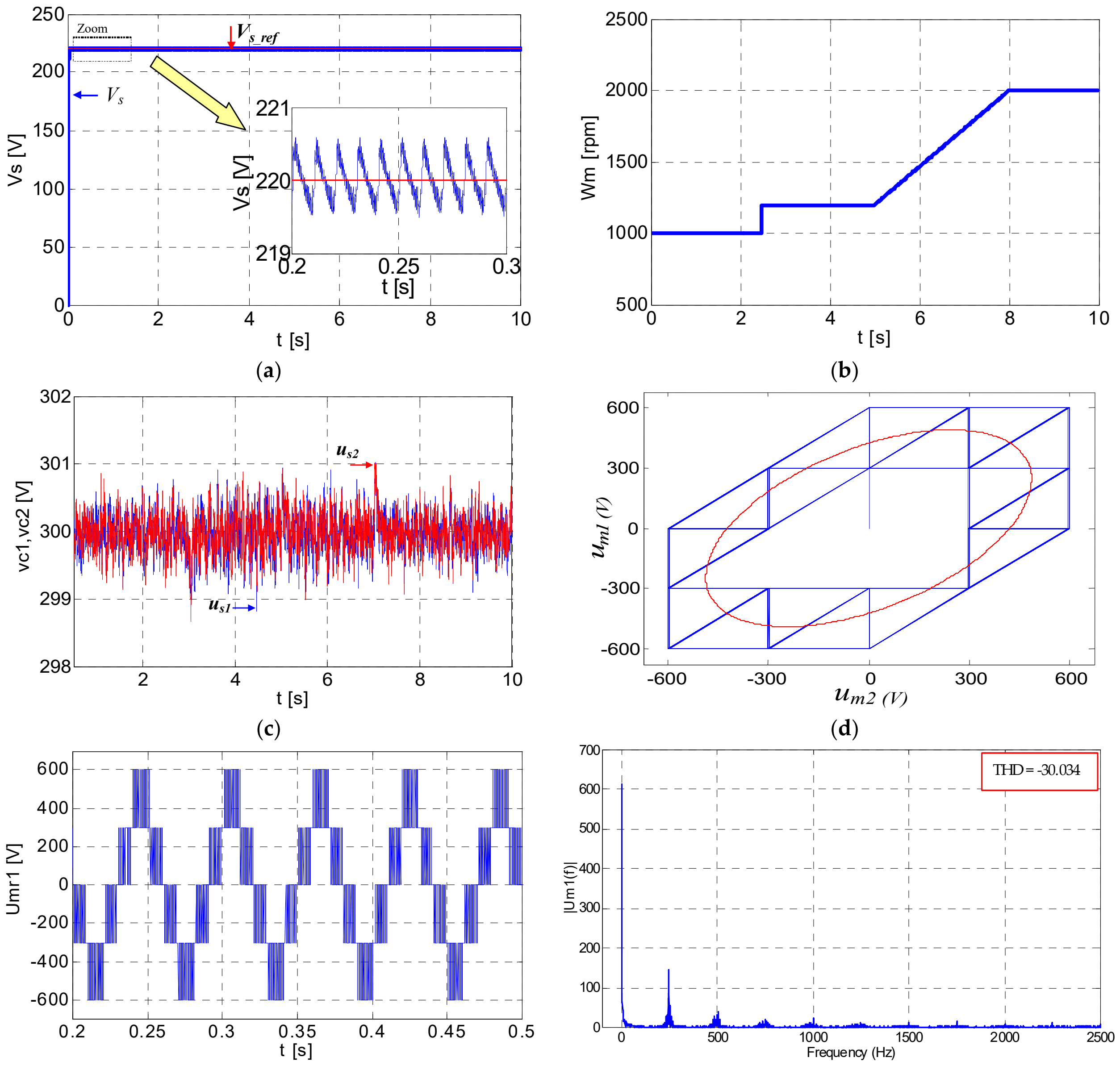

(**a**) (**b**) (**c**) (**d**) (**e**) (**f**)

Figure 12. The figure shows the simulation results of three-level NPC-converter-based standalone WECS control: (**a**) DFIG stator line-to-neutral rms voltage (reference and simulated); (**b**) wind turbine rotating speed; (**c**) voltage across the capacitors C_1 and C_2; (**d**) reference-modulated voltages and voltage vectors used for the three-level converter in the plan (u_{m1}, u_{m2}); (**e**) modulated line-to-line output voltage of the three-level NPC converter; and (**f**) single-sided amplitude spectrum of the line-to-line output voltage.

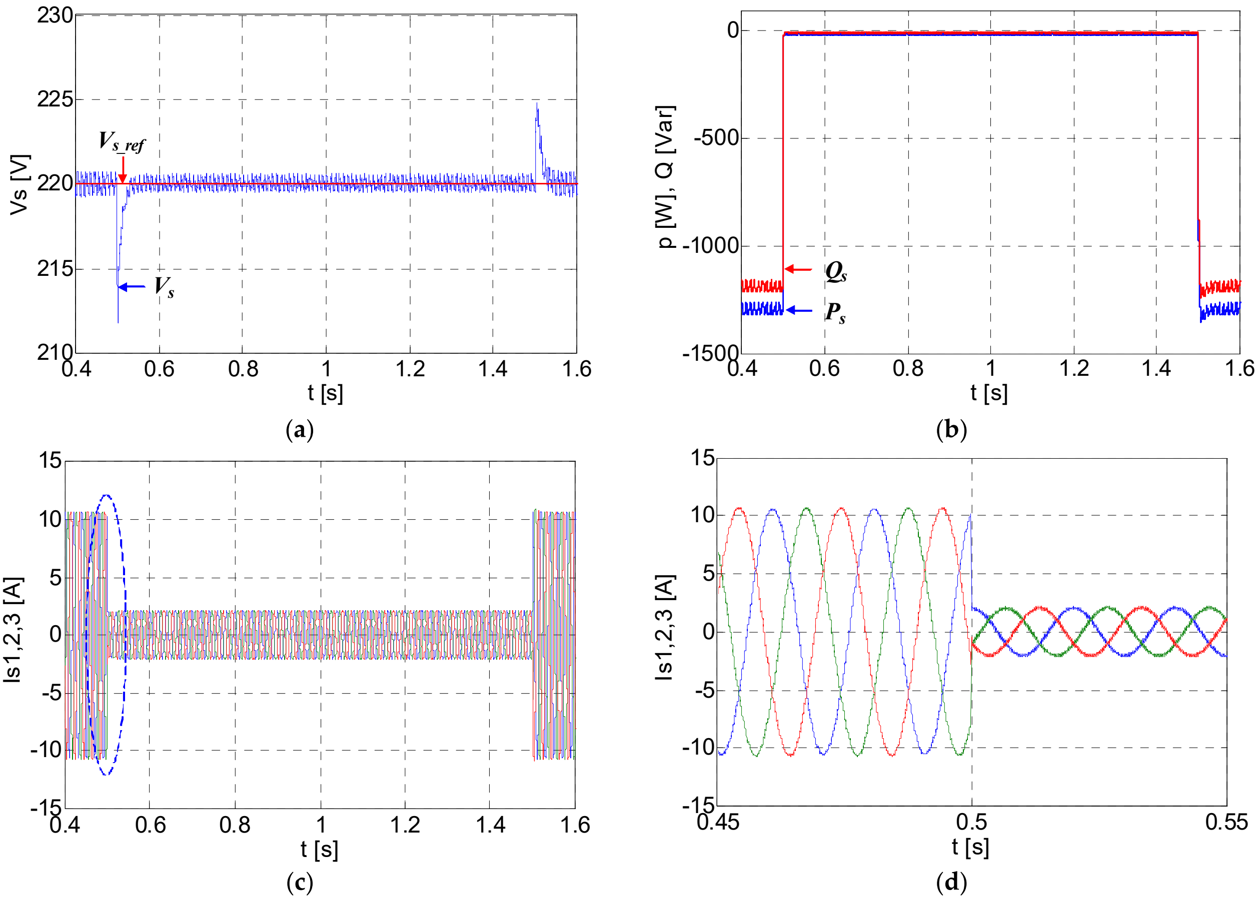

Figure 13. The figure shows the simulation results of the standalone WECS control with load variation: (**a**) DFIG stator line-to-neutral rms voltage (reference and simulated); (**b**) active and reactive powers produced by the DFIG to the load; (**c**) three-phase load currents; and (**d**) zoom of the three-phase load currents around time 1.5 s.

6. Experimental Results

A laboratory experimental test bench was built (Figure 14) to confirm the validity of the proposed SDSVM technique in controlling a three-level NPC converter supplying a simple three-phase load (Figure 14a). Then, this technique was implemented to control the voltage and frequency of the whole standalone DFIG-based WECS (Figure 14b), which consists of a wind turbine emulator based on a torque-controlled DC machine, a PMSM, a DFIG, and a three-level NPC converter. The last component was designed for 6 kVA drive operation, with 400 V, 50 Hz AC, and a DC voltage of us = 250 V with 1500 µF/350 V capacitors. The power modules were two bridged insulated gate bipolar transistors (IGBTs), which were packed into one module. Hall effect sensors were used to sense the required currents and voltages for the control method. The proposed SDSVM technique, as well as the standalone DFIG-based WECS control strategy, were both implemented on a dSPACE DS1104 board.

Figure 15 displays the experimental results of the three-level NPC controlled by the proposed SDSVM supplying a three-phase load. Figure 15a displays the modulated line-to-line voltages u_{m1}, the modulated line-to-neutral voltage v_{m1}, and the load current i_{L1}. Figure 15b shows the evolution of the DC link voltage u_s as well as voltages u_{s1} and u_{s2} across the upper and lower capacitors during the balancing procedure. It can be clearly seen that after time t_1 (the beginning time of the balancing procedure execution), the voltages of both capacitors converged to an equal value after 400 ms. This is due to the capability of the proposed SDSVM to adhere to the redundant NPC converter switching states. The angles θ (between the u_{m2}-axis and the reference voltage vector u_{mref}) and θ_c

(between the u_{m2}-axis and the new reference voltage vector u_{mref_c}) are shown in Figure 15c. In addition, Figure 15d shows the hexagon and the sector in which the voltage vector reference tip is located. It is clearly shown that hexagon H and sector S have a staircase shape and, therefore, the reference voltage vector will certainly sweep the six hexagons and the six sectors. Figure 15e illustrates the line-to-line output voltage together with its respective single-sided amplitude spectrum. Figure 15f shows the waveform of the line-to-line voltage, load current, and DC link voltage with a step change in the frequency (from 50 Hz to 100 Hz) of the voltage reference. This result confirms the validity of the SDSVM, even during a transient state.

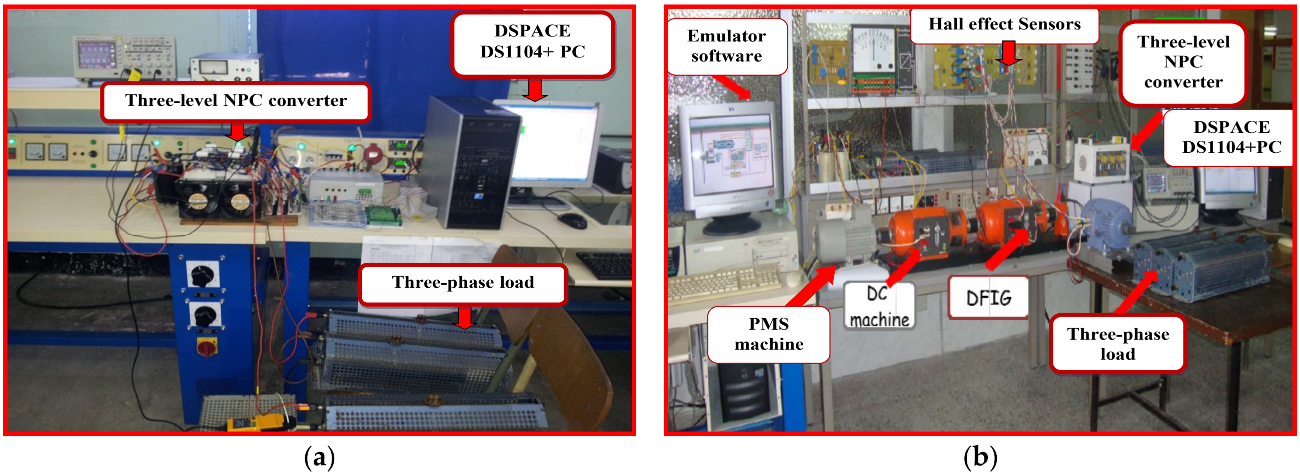

(**a**) (**b**)

Figure 14. The figure shows the laboratory experimental test bench: (**a**) experimental test bench of the three-level NPC converter supplying a three-phase load; (**b**) experimental test bench of the whole standalone three-level NPC-converter-based WECS.

To confirm the overall control of the standalone WECS when using the proposed SDSVM technique, we provided Figure 16. In fact, Figure 16a displays the steady-state waveforms of the three-level converter line-to-line output voltage, DFIG rotor current, DFIG stator current, and DFIG stator voltage. It is obvious that the rotor current frequency is smaller than that of the stator current. Figure 16b illustrates the used voltage vectors of the three-level NPC converter in the (u_{m1}, u_{m2}) plan.

From Figure 16c, it is clear that the rms output voltage and frequency have achieved their references even with load variation. This is due to the good control of the DFIG rotor current, and consequently, the output voltage of the NPC converter (Figure 16d). Thus, these results confirm the robustness of the control system even under load variation. It was noted that due to the load change, the voltage establishment time was 50 ms, and the frequency establishment time was 80 ms. Figure 16e,f illustrates the experimental waveforms of system control during step-up and step-down changes in the rms voltage reference, respectively. Moreover, it can be clearly seen that during these changes, the regulated rms voltage follows its reference. It can also be noted that the voltage establishment time due to the step-up change in the reference voltage is 160 ms, whereas, for the step-down change, it is 160 ms.

The results provided in this figure prove the efficiency of the proposed control for both steady and transient states.

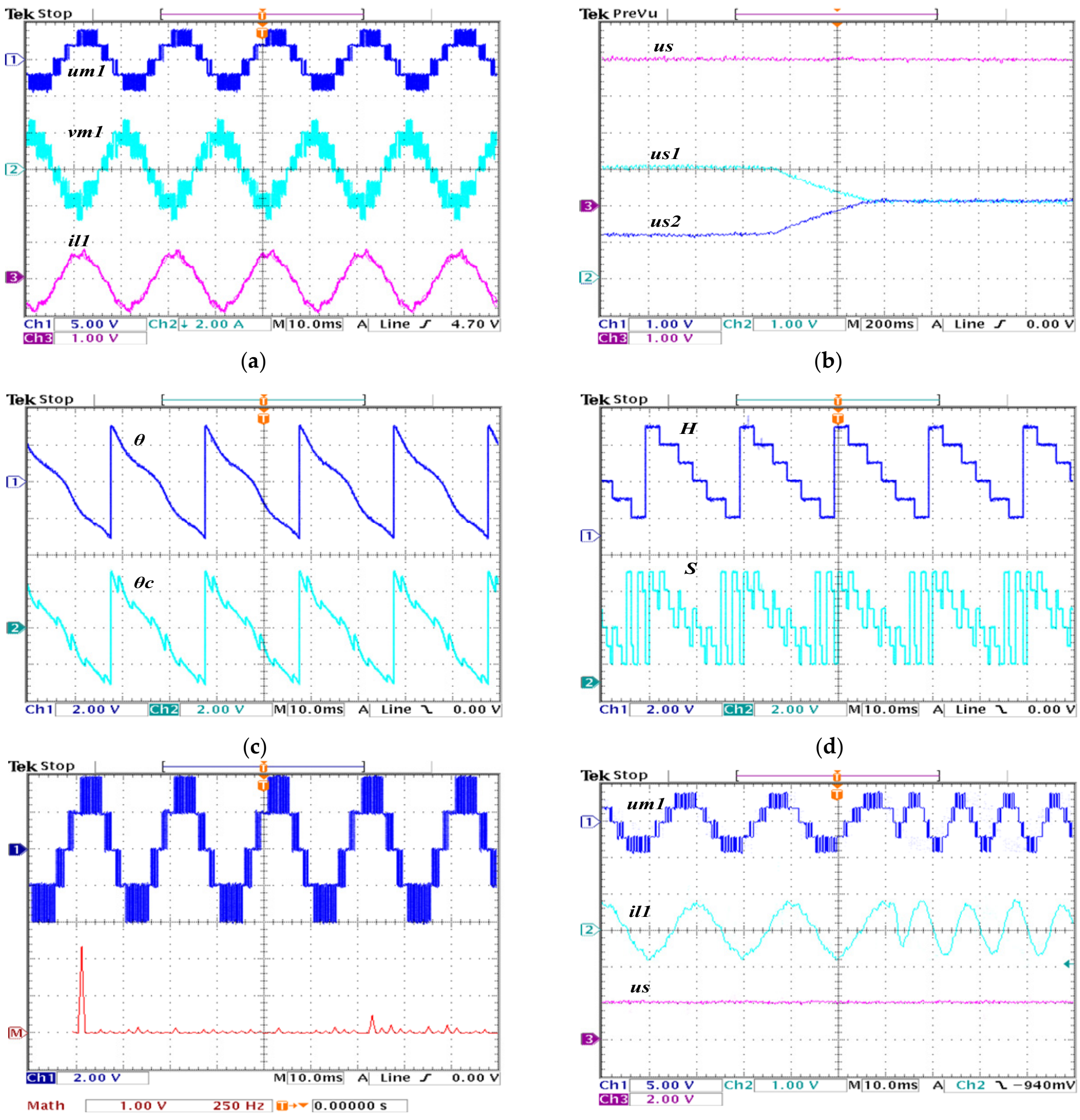

(**a**) (**b**) (**c**) (**d**) (**e**) (**f**)

Figure 15. The figure shows the experimental results of the three-level NPC controlled by the SDSVM supplying a three-phase load: (**a**) experimental waveforms of the line-to-line output voltage (200 V/div), line-to-neutral output voltage (200 V/div), and load current (3 A/div); (**b**) experimental waveforms of the DC link voltage (200 V/div), voltage across capacitor C_1 (200 V/div), and voltage across capacitor C_2 (200 V/div) during the balancing time; (**c**) angle evolution θ defining the hexagons, and angle evolution θ_c defining the sectors; (**d**) hexagons and sectors; (**e**) experimental waveforms of line-to-line output voltage (200 V/div) and single-sided amplitude spectrum; (**f**) experimental waveforms of line-to-line output voltages (200 V/div), load current (3 A/div), and DC link voltage (200 V/div) with a step change in frequency.

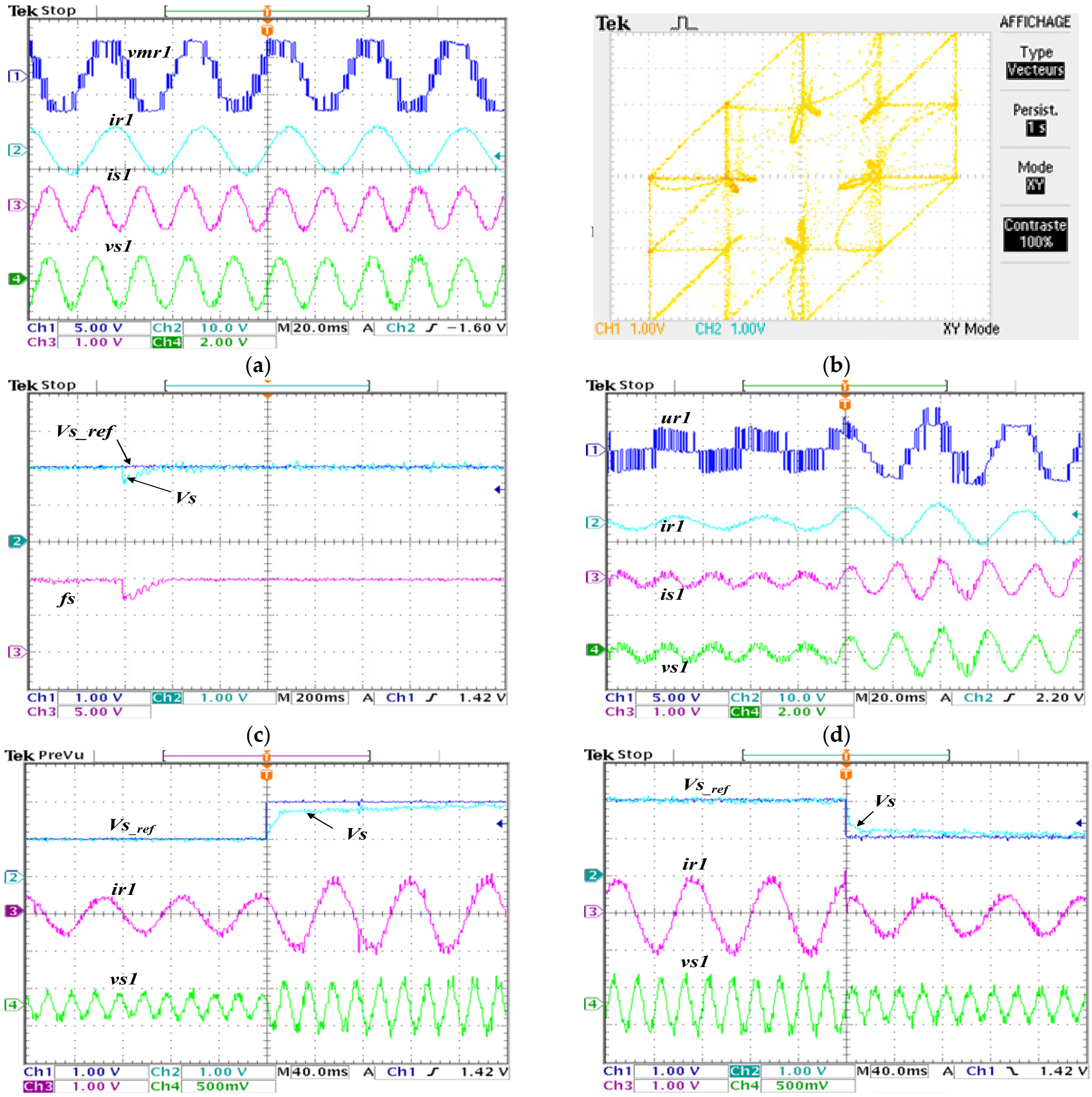

(**a**) (**b**) (**c**) (**d**) (**e**) (**f**)

Figure 16. The figure shows the experimental results of three-level NPC-converter-based standalone WECS control: (**a**) experimental waveforms of the three-level NPC converter line-to-line output voltage (200 V/div), DFIG rotor current (10 A/div), DFIG stator current (3 A/div), and DFIG stator voltage (200V/div); (**b**) used voltage vectors of the three-level NPC converter in the plane (u_{m1}, u_{m2}); (**c**) experimental waveforms of the reference rms voltage, regulated rms voltage (200V/div), and frequency (25 Hz/div); (**d**) experimental waveforms of the three-level NPC converter line-to-line output voltage (200 V/div), DFIG rotor current (10 A/div), DFIG stator current (3 A/div), and DFIG stator voltage (200 V/div) with load change; (**e**) experimental waveforms of the reference and measured output voltage (200 V/div), DFIG rotor current (10 A/div), and DFIG stator voltage (200 V/div) during step-up change of the voltage reference; (**f**) experimental waveforms of the reference and measured output voltages (200 V/div), DFIG rotor current (10 A/div), and DFIG stator voltage (200 V/div) during step-down changes in the voltage reference.

7. Conclusions

In this paper, the control of a standalone DFIG-based WECS using a three-level NPC converter has been presented. The main purpose of this work is to regulate the magnitude and frequency of the output voltage when supplying three-phase AC loads. In order to accomplish this task, the rotor currents of the DFIG were controlled by using the proposed SDSVM combined with two PI controllers. This technique provided ease of implementation since it allows us to copy directly modulated waveforms onto the output voltages of a three-phase, three-level converter without using a Park transformation. Furthermore, it also permits the simplification of the line-to-line space vector diagram of a three-level converter to that of a two-level converter. This SDSVM can be easily extended for use in high-order multilevel converters. The validity of the proposed technique for standalone DFIG-based WECS control was verified via simulation and validated with a laboratory experimental test bench of a three-level converter-based standalone WECS. The presented simulation and experimental results have confirmed the validity of the proposed SDSVM and demonstrated the good performance of the standalone DFIG-based WECS when using a three-level NPC converter.

Author Contributions: Methodology, T.G.; Software, T.G.; Validation, T.G.; Formal analysis, L.B., B.F. and S.B.; Resources, L.B. and N.R.; Writing—original draft, T.G.; Writing—review & editing, B.F.; Supervision, B.F. and S.B. All authors have read and agreed to the published version of the manuscript.

Funding: This research received no external funding.

Data Availability Statement: The original contributions presented in the study are included in the article, further inquiries can be directed to the corresponding author.

Conflicts of Interest: The authors declare no conflict of interest.

References

1. Zhang, C.; Wang, L.; Wu, X.; Gao, X. Performance analysis and design of a new-type wind-motor hybrid power pumping unit. *Electr. Power Syst. Res.* **2022**, *208*, 107931. [CrossRef]
2. Li, Z.L.; Li, P.; Yuan, Z.P.; Xia, J.; Tian, D. Optimized utilization of distributed renewable energies for island microgrid clusters considering solar-wind correlation. *Electr. Power Syst. Res.* **2022**, *206*, 107822. [CrossRef]
3. Behabtu, H.A.; Coosemans, T.; Berecibar, M.; Fante, K.A.; Kebede, A.A.; Mierlo, J.V.; Messagie, M. Performance evaluation of grid-connected wind turbine generators. *Energies* **2021**, *14*, 6807. [CrossRef]
4. Dannier, A.; Fedele, E.; Spina, I.; Brando, G. Doubly-fed induction generator (DFIG) in connected or weak grids for turbine-based wind energy conversion system. *Energies* **2022**, *15*, 6402. [CrossRef]
5. Porte-Agel, F.; Bastankhah, M.; Shamsoddin, S. Wind-turbine and wind-farm flows: A review. *Bound.-Layer Meteorol.* **2020**, *174*, 1–59. [CrossRef] [PubMed]
6. Ahmed, S.D.; Al-Ismail, F.S.M.; Shafiullah, M.; Al-Sulaiman, F.A.; El-Amin, I.M. Grid integration challenges of wind energy: A review. *IEEE Access* **2020**, *8*, 10857–10878. [CrossRef]
7. Ghennam, T. Supervision d’une Ferme Eolienne Pour son Intégration Dans la Gestion d’un Réseau Electrique, Apports des Convertisseurs Multi-Niveaux au Réglage des Eoliennes à Base de Machine Asynchrone à Double Alimentation. Ph.D. Thesis, École Centrale de Lille, Villeneuve-d’Ascq, France, EMP, Algiers, Algeria, 2010.
8. Ghennam, T.; Berkouk, E.M.; Francois, B. Modeling and Control of a doubly fed induction generator based wind conversion system. In Proceedings of the International Conference on Power Engineering, Energy and Electrical Drives (POWERENG 2009), Lisbon, Portugal, 18–20 March 2009.
9. Yaramasu, V.; Dekka, A.; JDurán, M.; Kouro, S.; Wu, B. PMSG-Based wind energy conversion systems: Survey on power converters and controls. *IET Electr. Power Appl.* **2017**, *11*, 956–968. [CrossRef]
10. Karad, S.; Thakur, R. Recent trends of control strategies for doubly fed induction generator based wind turbine systems: A comparative review. *Arch. Comput. Methods Eng.* **2021**, *28*, 15–29. [CrossRef]
11. Yaramasu, V.; Dekka, A.; Kourou, S. Multilevel converters for renewable energy systems. In *Multilevel Inverters, Control Methods and Advanced Power Electronics*; Academic Press: Cambridge, MA, USA, 2021; Volume 6, pp. 155–184.
12. Ghennam, T.; Berkouk, E.M.; Francois, B. A novel space vector current control based on circular hysteresis areas of a three-phase neutral-point-clamped inverter. *IEEE Trans. Ind. Electron.* **2010**, *57*, 2669–2678. [CrossRef]
13. Amjad, A.M.; Mehran, K.; Gadoue, S.; Blaabjerg, F. Online harmonic elimination pulse width modulation technique for modular multilevel cascade converter. *Int. J. Electr. Power Energy Syst.* **2021**, *133*, 107242. [CrossRef]
14. Ghennam, T.; Berkouk, E.M. Back-to-back three-level converter controlled by a novel space-vector hysteresis current control for wind conversion systems. *Electr. Power Syst. Res.* **2010**, *80*, 444–455. [CrossRef]
15. Espinoza, M.; Cárdenas, R.; Diaz, M.; Clare, J.C. An enhanced dq-based vector control system for modular multilevel converters feeding variable speed drives. *IEEE Trans. Ind. Electron.* **2017**, *64*, 2620–2630. [CrossRef]
16. Aguilera, R.P.; Acuña, P.; Lezana, P.G.; Konstantinou, G.; Wu, B.; Bernet, S.; Agelidis, V.G. Selective harmonic elimination model predictive control for multilevel power converters. *IEEE Trans. Power Electron.* **2017**, *32*, 2416–2426. [CrossRef]

17. Yang, S.; Tang, Y.; Wang, P. Distributed control for a modular multilevel converter. *IEEE Trans. Power Electron.* **2018**, *33*, 5578–5591. [CrossRef]
18. Liu, X.; Qiu, L.; Wu, W.; Ma, J.; Fang, Y.; Peng, Z.; Wang, D. Efficient model-free predictive power control for active front-end modular multilevel converter. *Int. J. Electr. Power Energy Syst.* **2021**, *132*, 107058. [CrossRef]
19. Francois, B.; Semail, E. Modeling and Control of a Three-Phase Neutral-Point-Clamped Inverter by Means of a Direct Space Vector Control of Line to Line Voltages. In Proceedings of the 10th European Power Electronics and Motion Control Conference (EPE-PEMC 2002), Cavtat & Dubrovnik, Croatia, 9–11 September 2002.
20. Ko, H.S.; Yoon, G.G.; Kyung, N.H.; Hong, W.P. Modeling and control of DFIG-based variable-speed wind-turbine. *Electr. Power Syst. Res.* **2008**, *78*, 1841–1849. [CrossRef]
21. Zamanifar, M.; Fani, B.; Golshan, M.E.H.; Karshenas, H.R. Dynamic modeling and optimal control of DFIG wind energy systems using DFT and NSGA-II. *Electr. Power Syst. Res.* **2014**, *108*, 50–58. [CrossRef]
22. Somoro, M.A.; Memon, Z.A.; Kumar, M.; Baloch, M.H. Wind energy integration: Dynamic modeling and control of DFIG based on super twisting fractional order terminal sliding mode controller. *Energy Rep.* **2021**, *7*, 6031–6043. [CrossRef]
23. Khatounian, F.; Monmasson, E.; Berthereau, F.; Delaleau, E.; Louis, J.P. Control of a doubly fed induction generator for aircraft application. In Proceedings of the IECON'03. 29th Annual Conference of the IEEE Industrial Electronics Society (IEEE Cat. No. 03CH37468), Roanoke, VA, USA, 2–6 November 2003; pp. 2711–2716.
24. Bekiroglu, E.; Yazar, M.D. MPPT Control of grid connected DFIG at variable wind speed. *Energies* **2022**, *15*, 3146. [CrossRef]
25. Behara, R.K.; Saha, A.K. neural network predictive control for improved reliability of grid-tied DFIG-based wind energy system under the three-phase fault condition. *Energies* **2023**, *16*, 4881. [CrossRef]
26. Chhipą, A.A.; Chakrabarti, P.; Bolshev, V.; Chakrabarti, T.; Alexey, G.S.; Vasilyev, N.; Ghosh, S.; Kudryavtsev, A. modeling and control strategy of wind energy conversion system with grid-connected doubly-fed induction generator. *Energies* **2022**, *15*, 6694. [CrossRef]
27. Aljafari, B.; Stephenraj, J.P.; Vairavasundaram, I.; Rassiah, R.S. Steady state modeling and performance analysis of a wind turbine-based doubly fed induction generator system with rotor control. *Energies* **2022**, *15*, 3327. [CrossRef]
28. Mesbahi, T.; Ghennam, T.; Berkouk, E.M. A doubly fed induction generator for wind stand-alone power applications (simulation and experimental validation). In Proceedings of the 2012 XXth International Conference on Electrical Machines, Marseille, France, 2–5 September 2012.
29. Ghennam, T.; Belhadji, L.; Francois, B.; Bacha, S. A simplified line-to-line space vector modulation for multilevel converter applied for a standalone wind energy conversion system. In Proceedings of the 21st European Conference on Power Electronics and Applications (EPE'19 ECCE Europe), Geova, Italy, 3–5 September 2019.
30. Akel, F.; Ghennam, T.; Laour, M.; Bendib, D.; Berkouk, E.M.; Chikh, M. Control of single stage grid connected pv-inverter based on direct space vector pwm. *Prog. Clean Energy* **2015**, *2*, 755–774.